Detecting Small Liver Tumors with ^{111}In-pentetreotide SPECT – A Collimator Study Based on Monte Carlo Simulations

Emma Mähler, Torbjörn Sundström, Jan Axelsson, and Anne Larsson, *Member, IEEE*

***Abstract*—In ^{111}In-pentetreotide single photon emission computed tomography (SPECT), the tumor to background uptake ratio is generally high. The noise is however also usually on a high level, and in combination with the low spatial resolution of SPECT, this may lead to difficulties in the detection of small tumors. This is especially the case in regions with a relatively high background activity, such as in the liver, which is a common region for somatostatin-positive metastases. To visually detect the small tumors is important for a successful treatment of the cancer disease. In this study we compare three different parallel-hole collimators for ^{111}In-pentetreotide SPECT regarding contrast as a function of image noise for a phantom simulating small tumors in liver background. The corresponding contrast-to-noise ratios are also presented. All raw-data projections are produced using Monte Carlo simulations. The collimators are of type low-energy general-purpose (LEGP), extended LEGP (ELEGP) and medium-energy general-purpose (MEGP). Reconstructions were performed with OSEM both with and without model-based compensation. Of the investigated collimators, the ELEGP collimator proved to be the most optimal for the smallest tumors, both with and without model-based compensation included in the reconstruction. It is also shown that model-based compensation outperforms the conventional reconstruction technique.**

***Index Terms*—^{111}In-pentetreotide, liver tumor, model-based compensation, SPECT**

I. Introduction

SOMATOSTATIN receptor scintigraphy (SRS) using ^{111}In-pentetreotide ([^{111}In-DTPA0]-octreotide, (OctreoScan), Tyco Healthcare, Mallickrodt, St Louis, USA) [1] is a well-established method which has a high accuracy for visualization of neuroendocrine tumors (NETs) and a great clinical impact on patient management [2], [3]. ^{111}In-pentetreotide is the most commonly used somatostatin analogue and single photon emission computed tomography (SPECT) imaging provides information for better staging and tumor follow-up. It also brings possibilities to predict radiotherapeutic efficiency and to perform dosimetry with somatostatin analogues such as [DOTA-Tyr3]-octreotide (DOTATOC) and [DOTA-Tyr3-Thr8]-octreotide (DOTATATE) labeled with beta-emitting radionuclides [4], [5].

^{111}In-pentetreotide SPECT has become a rather frequently performed study at the University Hospital of Umeå, with about 60 patient examinations per year. The patients are injected with about 160 MBq ^{111}In-pentetreotide day 1, and the SPECT examination is performed day 2, about 21 hours post-injection. The SPECT study is performed using an Infinia Hawkeye SPECT system, with two fields of view (FOV), one over the chest, and one over the abdominal region. The two FOVs are merged during reconstruction, resulting in one reconstructed image volume. The use of two FOVs is advantageous since the risk of missing unexpected tumors outside of the imaged region is reduced, but the risk of movement artifacts limits the acquisition time per FOV. A medium-energy general-purpose (MEGP) collimator is used for ^{111}In because of the higher energy emission of 245 keV. This collimator has a relatively low sensitivity, and combined with the relatively short acquisition time per FOV, the low amount of injected activity and the decay and clearance between injection and acquisition, the resulting images have relatively high noise levels compared to many other SPECT studies.

In a previous study from our research group the extended low-energy general-purpose (ELEGP) collimator proved to be the optimal collimator for ^{123}I-IBZM SPECT [6], when reconstructing with OSEM including model-based compensation. This collimator is developed for ^{81}Kr and ^{123}I and as can be seen in Table I, it combines a relatively high sensitivity with a septum thickness which is double that of the low-energy general-purpose (LEGP) collimator. ^{123}I-IBZM and ^{111}In-pentetreotide studies both suffer from high noise levels, and we were therefore interested to investigate if this

Manuscript received May 30, 2011. This work was supported by the University Hospital of Umeå.

Emma Mähler was with the Department of Radiation Sciences, Radiation Physics, Umeå University, SE-901 87 Umeå, Sweden, and is now with Gävle Hospital, Radiotherapy department, SE-801 87 Gävle, Sweden (e-mail: Emma.Mahler@lg.se).

Torbjörn Sundström is with the Department of Radiation Sciences, Diagnostic Radiology, Umeå University, SE-901 87 Umeå, Sweden (e-mail: Torbjorn.Sundstrom@diagrad.umu.se).

Jan Axelsson is with the Department of Radiation Sciences, Radiation Physics, Umeå University, SE-901 87 Umeå, Sweden (e-mail: Jan.E.Axelsson@vll.se).

Anne Larsson is also with the Department of Radiation Sciences, Radiation Physics, Umeå University, SE-901 87 Umeå, Sweden (e-mail: Anne.Larsson@vll.se, phone: +4690 785 24 87, fax: +4690 785 15 88)

collimator also could improve ^{111}In-pentetreotide imaging. In contrast to the previous study, we were however not interested in any quantitative measures of activity uptake, but only to visually detect the tumors as done in clinical practice at the University Hospital of Umeå. The most challenging tumors to detect are small tumors in high activity backgrounds, such as the liver. The liver is also a common region for somatostatin-positive metastases, and to visually detect these as early as possible is important for a successful treatment of the cancer disease.

For detection of small tumors, ^{111}In-pentetreotide SPECT should benefit from iterative reconstruction techniques which include models for image degrading effects. This includes correction for non-homogeneous attenuation, scatter, collimator detector response (CDR), and septal scatter and penetration (hereafter combined in the term septal penetration) which is important for ^{111}In when using low energy collimators. It could also include corrections for partial volume effects although these are not used in this study. Model-based compensation for scatter and septal penetration does not lead to the same increase in noise as subtraction-based techniques [7], [8], and CDR compensation improves image quality with respect to noise and image resolution [9]. Model-based compensation is frequently used for research, and can also be used in clinical routine studies, although the introduction has been rather slow.

The aim of this study was to compare the MEGP and ELEGP collimators for detection of small tumors in liver background. For comparison, the LEGP collimator was also included. The evaluation is performed using tumor contrast as a function of background noise, since the collimator showing the highest contrast for a certain background noise level should be the most optimal for detecting the tumors. We also include a contrast-to-noise (CNR) measure, as a function of iteration number, for a more direct comparison of contrast and noise. CNR can also give some guidance to the optimal number of iterations. Another aim of the study was to compare results from OSEM including model-based compensation to a conventional OSEM reconstruction technique including correction for attenuation, with and without scatter correction with a subtraction-based technique.

II. Materials and Methods

A. Digital phantom

For the Monte Carlo simulations, we decided to use a simple geometry in which relevant statistics could be retrieved using regions of interest (ROIs) in a single image. A digital cylindrical phantom consisting of tumor-like spheres in a homogeneous background corresponding to uptake of the radiopharmaceutical in liver was therefore chosen, and can be seen in Fig. 1. The length of the phantom was set to 25.0 cm and its diameter was determined from patient images, as described below. The phantom contains spheres of two sizes, ten spheres with a diameter of 12 mm, hereafter called S12, and eight spheres with a diameter of 20 mm, hereafter called S20, symmetrically located at opposite ends of the cylinder. The smaller size of the spheres was chosen from "trial-and-error" simulations, where 12 mm proved to be a size that at best was barely visible in realistic conditions with the conventional reconstruction technique. We were however also interested in how collimator choice and reconstruction methods affect images of somewhat larger tumors, and we therefore used spheres of 20 mm in diameter at the other end of the phantom. The S12 sphere centers were placed 5.5 cm from the phantom edge in the YZ-plane and 5.1 cm in the X direction, according to the coordinate system in Fig. 1. The S20 sphere centers were placed 5.5 cm from the phantom edge in YZ-plane and 5.5 cm in the X direction. The phantom was centered at the origin of the simulated gamma camera system.

To make the phantom correspond to a realistic ^{111}In-pentetreotide SPECT study, a set of 20 anonymized patient images from the Nuclear Medicine Department at the University Hospital of Umeå was selected. 10 of the patients had been diagnosed with somatostatin-positive metastases in the liver and 10 were without visible liver disease. All images had been acquired with a MEGP collimator. According to the clinical protocol, two FOVs had been acquired, each with 60 equally spaced projection angles in a 360º stepwise rotation and a time per view of 30 s. An elliptical orbit had been used with automatic body contour detection. Data were acquired in two 20% windows centered around each of the two ^{111}In emission energies at 171 and 245 keV. A scatter window between 127 and 153 keV was also used. The images had been reconstructed on the clinical workstation (Xeleris 2.1220, General Electric, WI, USA), according to the clinical protocol based on OSEM (2 iterations, 10 subsets) including correction for non-homogeneous attenuation using Hawkeye computed tomography (CT) images and scatter correction with the Compton window method. Post-filtering with a 3D Butterworth filter (critical frequency 0.40 cm^{-1}, power factor 8) had also been performed.

For determination of the tumor to background ratio, the 15 largest liver tumors were used, which all had a diameter that clearly exceeded 3.0 cm. An approximate value of uptake was measured by using a region of interest (ROI) over the tumor in the transaxial slice where the tumor showed its maximum intensity. The maximal value in the ROI was determined, and was used for the uptake measure, to minimize influences from partial volume effects. A ROI in what was considered as healthy liver tissue was used for the background comparison, and in that case the average ROI value was used. The average tumor to background ratio was then calculated to 11.3 (± 3.0) for the 15 tumors, and the sphere to background ratio in the phantom was set to this value.

The patient images were also used to determine an average number of the counts per pixel from the liver, which is needed for determining a realistic noise level in the projection images. The images of the patients without visible liver disease were used, and one of the projection images, facing the liver from the anterior side, was selected. A ROI was placed over a

homogeneous and thick part of the liver, avoiding other organs, and the average value of counts per pixel was corrected for attenuation from overlying tissue which thickness was determined from the Hawkeye CT images. The corrected average number of counts per pixel for all 10 patients was calculated to 13.8 (± 4.5) and according to the theory of Poisson statistics, the inverted square root of this average value was assumed to be a representative level of relative image noise in the projection images. This method for determining noise is crude since other tissues contribute to the counts in the ROI to some degree. We did however verify the noise in the reconstructed phantom images against the reconstructed clinical patient images and it was found to correspond within a standard deviation of the patient variations.

The Hawkeye CT images for all patients were used when determining the diameter of the phantom. A representative slice of the liver was chosen, and the ant-post and lateral diameter of the patient was measured using geometrical tools in Xeleris. These diameters were averaged, and the average diameter for all patients, 28.6 cm, was used for the phantom.

B. Simulation

Monte Carlo simulations of the phantom were performed with SIMIND version 4.9 [10], [11] with parameters corresponding to an Infinia gamma camera (General Electric, WI, USA) with 0.95 cm thick NaI crystals, equipped with three different parallel-hole collimators: MEGP, ELEGP and LEGP. The characteristics of these collimators can be seen in Table I. The simulated isotope was ^{111}In and two energy windows of 20% were centered at 171 and 245 keV, respectively. The Compton window (127 to 153 keV) which is used clinically for subtraction-based scatter correction was also included. The images were simulated in 128 × 128 pixel matrices with a pixel size of 0.442 cm × 0.442 cm. 8×10^8 photons per projection were simulated, which resulted in images with a low noise level.

SIMIND uses several types of variance reduction techniques in order to reduce the computing time, and a consequence of this is that realistic Poisson noise in the SPECT projections is not possible to simulate directly. In this study, Poisson noise was therefore added to the simulated projection images. A similar procedure as in previous studies from our research group was used [6], [8]. For the MEGP collimator, a 20×20 pixel ROI was centered on one of the projection images of the cylinder, and the average number of counts/pixel was normalized to the corresponding value for the attenuation corrected liver measurements described above. Poisson noise was then generated using the function "imnoise" in Image Processing Toolbox, Matlab version R2010a (The Mathworks, Inc., MA, USA). For the other collimators the total number of counts was scaled using a factor derived from the total number of counts in each simulated SPECT image series compared to the corresponding MEGP simulation. Poisson noise was then generated for the scaled images.

C. Reconstruction

The reconstructions without model-based compensation were performed using the clinical protocol on the workstation Xeleris. Reconstructions were performed with 2, 3, 4, 6, 8, 10, 15 and 20 OSEM iterations with 10 subsets. All images were post-filtered with a Butterworth filter with a critical frequency of 0.40 cm^{-1} and a power factor of 8. The reconstructions were performed both with and without scatter correction with the Compton window method. No filtering of the scatter image was performed before scatter subtraction since this function is not available in the clinical protocol for reconstruction of two FOVs. When attenuation correction was used, it was based on a cylindrical attenuation map with different attenuation coefficients, depending on collimator and if scatter correction was included or not. The values used are presented in Table II. The linear attenuation coefficient of water 0.138 cm^{-1}, which was determined from simulations, was used for the MEGP reconstruction including scatter correction, where the effect of septal penetration is low. For the corresponding MEGP reconstruction without scatter correction we used an effective "broad-beam" attenuation coefficient, 0.092 cm^{-1}, also determined from simulations. For the ELEGP reconstructions without model-based compensation, the proper attenuation coefficient is more difficult to determine because of the effect of septal penetration of the primary photons. This effect depends on photon energy, collimator geometry, source distribution and distance from the collimator, and leads to a relative over-compensation in the central part of the images. We therefore used approximate attenuation coefficients determined from a "trial-and-error" process of testing different attenuation coefficients for achieving a homogeneous cylinder after reconstruction. Circular ROIs in reconstructed images in the homogeneous part of the phantom, far from the spheres in the X-direction, were used for this purpose. It should be mentioned that this method is difficult to apply for patient imaging, and that the values in Table II for the ELEGP collimator are only valid for this phantom. For the LEGP reconstructions, attenuation correction was discarded due to the already heavily over-compensated region in the centre of the reconstructed images.

Reconstructions including model-based compensation were performed with the software OSEMS, which is developed at John Hopkins University, Baltimore, USA. The software is based on OSEM and includes correction for attenuation, scatter, CDR and septal penetration. Images were saved for every iteration step up to 40, and 10 OSEM subsets were used. Evaluation was performed manually, and we selected the following numbers of iterations for evaluation: 2, 3, 4, 6, 8, 10, 15, 20, 25, 30 and 40. Scatter correction was performed using ESSE [12], with kernels simulated using SIMIND. The CDR compensation includes the effect of collimator penetration [13] and the table of response functions needed for this correction was also generated using SIMIND. The images were post-filtered with the same Butterworth filter as described above. Attenuation was corrected for using a cylindrical homogeneous attenuation map. The linear

attenuation coefficient of water, 0.138 cm^{-1}, was used for all model-based reconstructions since the degrading effect of scatter and septal penetration can be assumed to be properly corrected for.

D. Evaluation

To measure the image quality parameters, contrast and noise, the inhouse software Imlook4d was used. ROIs were drawn manually in a high quality "hot spot"-image (spheres simulated without background activity) and were then saved so that the same ROIs could be used for all reconstructions. For the small spheres, a ROI size of 9 pixels was used, and for the large spheres the corresponding ROI size was 25 pixels. Both ROI types were quadratic in shape which is a good approximation for a circle for the small ROI-size, and had an area corresponding to 1.55 times the cross section of the spheres. For the background, from which we also determined the noise, a ring-shaped ROI was placed in four homogeneous slices between the two sphere-ends of the phantom. The ring was approximately 2 cm wide in plane, and was placed so that it would have covered both the larger and smaller spheres if put in the same slice. It is therefore a good representation of the background around the spheres, which is important for the LEGP images which suffer from poor uniformity due to the high level of septal penetration.

The contrast, c, for each sphere was calculated as:

$$c = \frac{\bar{s} - \bar{b}}{\bar{b}} \quad (1)$$

where $\bar{s}$ is the mean count in the sphere ROI and $\bar{b}$ is the mean value of the four background ROIs. An average value for all the ROI values from spheres of the same size was then calculated. A standard error for the average value was calculated as the standard deviation of the variations in ROI-values, divided by the square root of the number of spheres.

The relative noise, N, in the background ROI was calculated as:

$$N = \frac{\sigma_b}{\bar{b}} \quad (2)$$

where σ_b is the standard deviation in a background ring-shaped ROI. An average N value of the four ROIs was used. Contrast was plotted as a function of noise for each OSEM-iteration for the different collimators and reconstruction methods.

The contrast-to-noise ratio for each sphere, CNR, was then calculated as:

$$CNR = \frac{\bar{s} - \bar{b}}{\sigma_b}. \quad (3)$$

The CNR was plotted as a function of OSEM-iteration in a similar manner.

III. Results

Contrast as a function of noise and the corresponding CNR as a function of iteration number for the conventional reconstruction technique are presented in Fig. 2. For S12 (Fig. 2a-b) it can be seen that the standard errors are relatively high, up to 16% in relative numbers for the MEGP collimator contrasts, including scatter correction. This is also the impression when studying the images, which are presented in Fig. 3, where some of the spheres are clearly visible and some of the spheres are not. For S20 (Fig. 2c-d), the standard errors are considerably smaller, up to 6% in relative numbers for the MEGP collimator contrasts, including scatter correction. Despite the high standard errors for S12, the average values in Fig. 2 follow a smooth curve, and the figure clearly demonstrates that OSEM reduces the bias and increases the noise from one iteration to the next.

When comparing the collimators in Fig. 2, it is obvious that the LEGP collimator gave the worst results, which also was expected. This is because of the high level of septal penetration. When comparing the other two collimators, the ELEGP collimator has the highest contrast for a certain noise level for the S12 spheres, which also results in the highest CNRs. The ELEGP collimator also shows somewhat lower standard errors compared to MEGP. If scatter correction has a positive influence or not for the S12 spheres is not totally clear because of the high standard errors. In Fig. 3, images with and without scatter correction can be compared, and the differences in sphere detection are not obvious. For the S20 spheres it is however clear from Fig. 2d that the highest CNRs are achieved when omitting scatter correction. From a CNR perspective, ELEGP without scatter correction is the best choice, but MEGP with scatter correction results in the highest contrasts, at the expense of noise.

When reconstruction is performed with model-based compensation, the pattern changes to some extent as can be seen in Fig. 4. The contrasts are generally a factor of 2-4 times higher than for the conventional reconstruction technique, and this is also the case for the CNR measure. When comparing the collimators, the ELEGP collimator is also in this case a better choice than the MEGP collimator. As can be seen in Fig. 4a and 4c, the contrast for the LEGP collimator converges at a higher level compared to the other collimators, but the convergence is slower. The CNR for this collimator is lower for the S12 spheres, but comparable to the ELEGP results for the S20 spheres, after about 10 iterations. In Fig. 5, images of the S12 spheres are presented for all collimators, for the number of iterations which results in the highest CNRs (left column) and highest contrasts (right column). In Fig. 5e for the LEGP collimator we chose however to present the peak value at 15 iterations (from Fig. 4b) instead of the slightly higher CNR at 2 iterations since the 2-iteration image gave a rather inhomogeneous impression that may result from a too low level of convergence.

The CNR can give some guidance to the number of iterations that is most optimal for detection of the spheres, and

for the conventional reconstruction technique, the highest CNRs are found for the lowest number of iterations that we included, which is 2. This is however not the case for the LEGP collimator, but due to the poor results, this collimator is of no interest for conventional reconstruction. For model-based compensation, the number of iterations that gives the highest CNR depends on collimator and sphere size. For S20, 2 iterations result in the highest CNR for ELEGP and MEGP, whereas 8 iterations is the optimum for LEGP. For S12, the highest CNR varies between 2 and 4 iterations but as mentioned, LEGP also has a peak at 15 iterations.

IV. Discussion

In this study the MEGP, ELEGP and LEGP collimators have been compared for detection of small spheres in a background corresponding to liver uptake of ^{111}In-pentetreotide. The MEGP collimator is the traditional choice for ^{111}In SPECT because of the medium-energy emission at 245 keV. For reconstructions without model-based compensation, this collimator is probably also the most optimal one if quantitative measures of activity concentrations are of interest, because of the low level of septal penetration. In this study we were however more interested in tumor detection, and the intensity difference between tumor and background, that is the contrast, is then the most important parameter. The detection is however limited by background noise, and for small tumors the tumor size is comparable to the correlation length of image noise in the reconstruction. It is therefore a risk that the tumor drowns in the high noise surroundings. Contrast as a function of noise was used, since it was assumed that the collimator showing the highest contrast for a certain noise level should be the most optimal for detecting the tumors. CNR as a function of iteration number was also calculated for a more direct comparison of contrast and noise. We are however aware that CNR can be seen as a crude measure of image quality, and that other analyses such as receiver operating characteristic (ROC) plots could have given additional valuable information. The objective assessment of image quality lies however beyond the scope of this paper. Also, in many cases the differences in lesion visibility were rather self-evident from the images in this study and subtle detection performance differences that would be quantified by using more sophisticated measures are not needed in such cases. The aim of the study was also to compare results from model-based compensation to a conventional reconstruction technique.

All reconstructed images in the study were filtered with a 3D Butterworth post-filter with a critical frequency of 0.40 cm^{-1} and a power factor of 8. This filter is what we use in the clinical routine for ^{111}In-pentetreotide images. To include other filters in the comparison would have been interesting, but beyond the scope of this study. We believe however that the collimator comparison would be similar for other filters, at least for other Butterworth filters with the same power factor. In a previous study from our research group [6] the relative differences between the collimators were roughly the same for the different Butterworth critical frequencies included in the comparison. Images without filtering were also included in that study and showed similar results. Based on the previous study we also believe that a lower critical frequency would result in a CNR peak at a higher number of iterations. If a higher number of iterations is desired for a better convergence, a lower critical frequency could therefore be considered.

The study was based on small ROIs that were copied to the reconstructed images. We chose ROIs and not volumes of interest (VOIs) for the contrast measure, for simplicity. We wanted the setup to be as realistic as possible, and the pixel size in the simulated phantom images is therefore the same as in a clinical ^{111}In-pentetreotide image, 0.442 cm × 0.442 cm. This means that it was difficult to centre the ROIs at the exact centre of the spheres, and to some degree this contributes to the high standard errors for the S12 spheres. To partly compensate for this we used 1.55 times larger ROIs than the cross-section of the spheres, which ensured that the hottest region was within the ROI. If VOIs had been used, the standard errors would probably have been somewhat smaller, but nothing points to that the conclusions would have been different. The S20 sphere results have relatively small standard errors, and show a similar pattern compared to the S12 results.

For the collimator comparison, the ELEGP collimator seems to be the most optimal choice for detecting the S12 spheres, and this is true both with and without model-based compensation. For the high noise levels that were simulated in this study, the higher sensitivity of the ELEGP collimator is clearly the decisive factor. For model-based compensation this was expected since it has been shown in other studies [14]-[16], [6] that a high sensitivity is positive for lesion detectability, contrast and quantitative accuracy. From Fig. 4d it is however clear that the highest contrasts achieved in this study are for the LEGP collimator. However, the convergence is slow, and from a CNR perspective the collimator can not be recommended for small tumor detection. Nevertheless, the results are interesting since it seems that the CDR method used in this work, which also includes the effect of septal penetration, can handle very high levels of septal penetration. The high LEGP contrasts also indicate that the high sensitivity which is positive when using model-based compensation not necessarily has to be based on only the correctly collimated photons. As can be seen in Table I, LEGP has a lower sensitivity than ELEGP for the correctly collimated photons, but a much higher sensitivity in total.

When comparing Fig. 3 and 5, it is obvious that the use of model-based compensation is a clear advantage for small tumor detection. For the MEGP collimator, the resolution modeling included in the CDR compensation has to be the most contributing part to the differences. For the LEGP collimator the correction for septal penetration, which also is included in the CDR compensation, is obviously very important. Other studies comparing reconstructions with and

without CDR compensation have also shown large differences [9], [15], [17]. The ESSE scatter correction which is included in the model-based compensation is also a contributor to the better results since it has been shown that such techniques do not lead to the same noise increase as subtraction-based techniques. The effect of better scatter correction is however likely to be rather small compared to the effect of CDR compensation.

The increase in CNR when using model-based compensation was as high as a factor of 2-4 in this study. The phantom represents however a piecewise constant rather simple geometry, and it is not certain that the increase would be this substantial for a more complex geometry with slower OSEM convergence. We have however no reason to believe that the simplicity of the phantom should affect the collimator comparison.

V. Conclusion

For ^{111}In-pentetreotide SPECT in high noise conditions, the ELEGP collimator is most optimal for detection of small spheres in liver background for OSEM reconstructions, both with and without model-based compensation. For larger tumors, the choice of collimator is more complex, but not as important since the larger spheres always were visible in this study, regardless of collimator and reconstruction method. Model-based compensation outperformed the conventional reconstruction technique and this study really points to the urgency of including model-based compensation in the clinical routine for ^{111}In-pentetreotide SPECT.

References

[1] E. P. Krenning, W. H. Bakker, P. P. Kooij, W. A. Breeman, H. Y. Oei, M. de Jong, *et al.,* "Somatostatin receptor scintigraphy with indium-111-DTPA-D-Phe-1-octreotide in man: metabolism, dosimetry and comparison with iodine-123-Tyr-3-octreotide," *J. Nucl. Med.,* vol. 33, no. 5, pp. 652-658, 1992.

[2] G. Cadiot, G. Bonnaud, R. Lebtahi, L. Sarda, P. Ruszniewski, D. Le Guludec, and M. Mignon, "Usefulness of somatostatin receptor scintigraphy in the management of patients with Zollinger-Ellison syndrome. Groupe de Recherche et d'Etude du Syndrome de Zollinger-Ellison (GRESZE)," *Gut,* vol. 41, no. 1, pp. 107-114, 1997.

[3] A. Sundin, U. Garske, and H. Orlefors, "Nuclear imaging of neuroendocrine tumours," *Best. Pract. Res. Clin. Endocrinol. Metab.,* vol. 21, no. 1, pp. 69-85, 2007.

[4] M. de Jong, W. A. Breeman, D. J. Kwekkeboom, R. Valkema, and E. P. Krenning, "Tumor imaging and therapy using radiolabeled somatostatin analogues," *Acc. Chem. Res.,* vol. 42, no. 7, pp. 873-880, 2009.

[5] D. J. Kwekkeboom, W. W. de Herder, and E. P. Krenning, "Somatostatin receptor-targeted radionuclide therapy in patients with gastroenteropancreatic neuroendocrine tumors," *Endocrinol. Metab. Clin. North Am.*, vol. 40, pp. 73-85, 2011.

[6] A. Larsson, S. Jakobson Mo, M. Ljungberg, and K. Riklund, "Dopamine D2 receptor SPECT with (123)I-IBZM: evaluation of collimator and post-filtering when using model-based compensation - a Monte Carlo study," *Phys. Med. Biol.,* vol. 55, pp. 1971-1988, 2010.

[7] E. C. Frey, B. M. W. Tsui, and M. Ljungberg, "A comparison of scatter compensation methods in SPECT: Subtraction-based techniques versus iterative reconstruction with accurate modeling of the scatter response," *Nuclear Science Symposium and the Medical Imaging Conference Conference Record*, pp. 1035-1037, 1992.

[8] A. Larsson, M. Ljungberg, S. Jakobson Mo, K. Riklund, and L. Johansson, "Correction for scatter and septal penetration using convolution subtraction methods and model-based compensation in ^{123}I brain SPECT imaging – A Monte Carlo study," *Phys. Med. Biol.,* vol. 51, pp. 5753-5767, 2006.

[9] B. F. Hutton and Y. H. Lau, "Application of distance dependent resolution compensation and post-reconstruction filtering for myocardial SPECT," *Phys. Med. Biol.*, vol. 43, pp. 1679-1693, 1998.

[10] M. Ljungberg and S. E. Strand, "A Monte Carlo program for the simulation of scintillation camera characteristics," *Comp. Meth. and Progr. in Biomed.*, vol. 29, pp. 257-72, 1989.

[11] M. Ljungberg, A. Larsson, and L. Johansson, "A new collimator simulation in SIMIND based on the Delta-Scattering technique," *IEEE Trans. Nucl. Sci.*, vol. 52, pp. 1370-5, 2005.

[12] E. C. Frey and B. M. W. Tsui, "A new method for modelling the spatially-variant, object-dependent scatter response function in SPECT," *IEEE Nuclear Science Symposium. Conference Record*, vol. 2, pp. 1082-6, 1996.

[13] M. Ljungberg, K. Sjögreen, X. Liu, E. Frey, Y. Dewaraja, and S. E. Strand, "A 3-dimensional absorbed dose calculation method based on quantitative SPECT for radionuclide therapy: evaluation for (131)I using Monte Carlo simulation," *J. Nucl. Med.*, vol. 43, pp. 1101-9, 2002.

[14] C. Kamphuis, F. J. Beekman, and B. F. Hutton, "Influence of collimator hole dimensions on parallel and cone-beam brain SPECT," *IEEE Nuclear Science Symposium Conference Record*, vol. 2, pp. 1047-1051, 1999.

[15] Y. H. Lau, B. F. Hutton and F. J. Beekman, "Choice of collimator for cardiac SPET when resolution compensation is included in iterative reconstruction," *Eur. J. Nucl. Med.*, vol. 28, pp. 39-47, 2001

[16] G. L. Zeng and G. T. Gullberg, "A Channelized-Hotelling-Trace Collimator Design Method Based on Reconstruction Rather Than Projections," *IEEE Trans. Nucl. Sci.*, vol. 49, pp. 2155-8, 2002.

[17] B. He, Y. Du, X. Song, W. P. Segars, and E. C. Frey, "A Monte Carlo and physical phantom evaluation of quantitative In-111 SPECT," *Phys. Med. Biol.,* vol. 50, pp. 4169-85, Sep. 2005

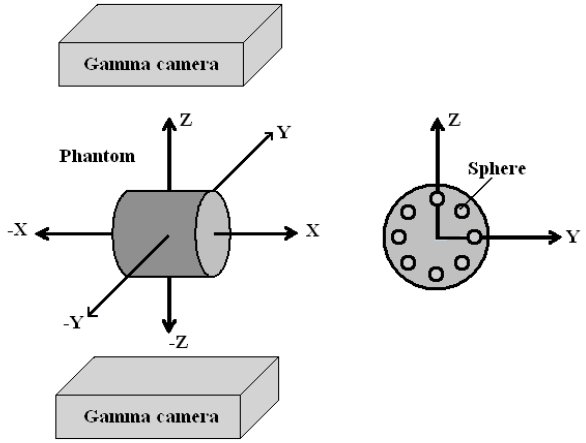

Fig. 1 The phantom and the coordinate system of the simulated gamma camera system.

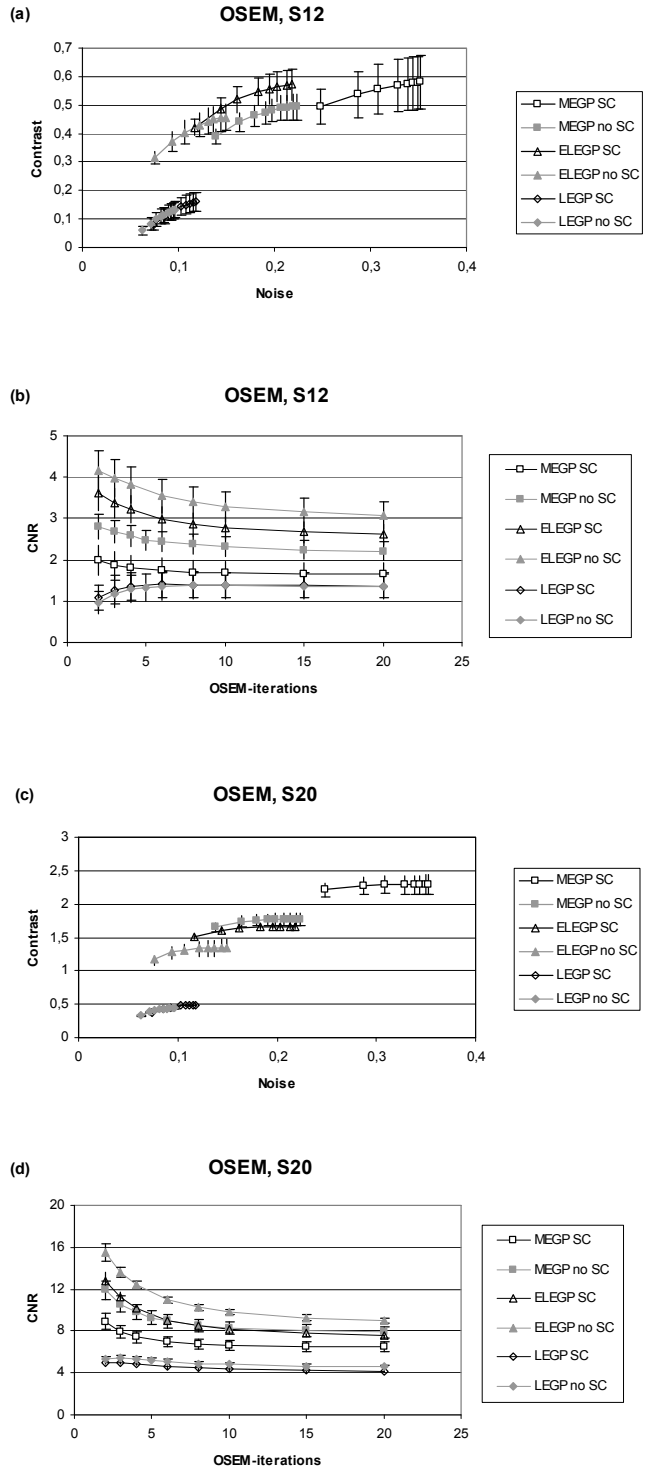

Fig. 2 a-d Contrast and CNR for the simulated phantom spheres for reconstructions without model-based compensation. The error bars show the standard errors for the spheres. SC stands for scatter correction.

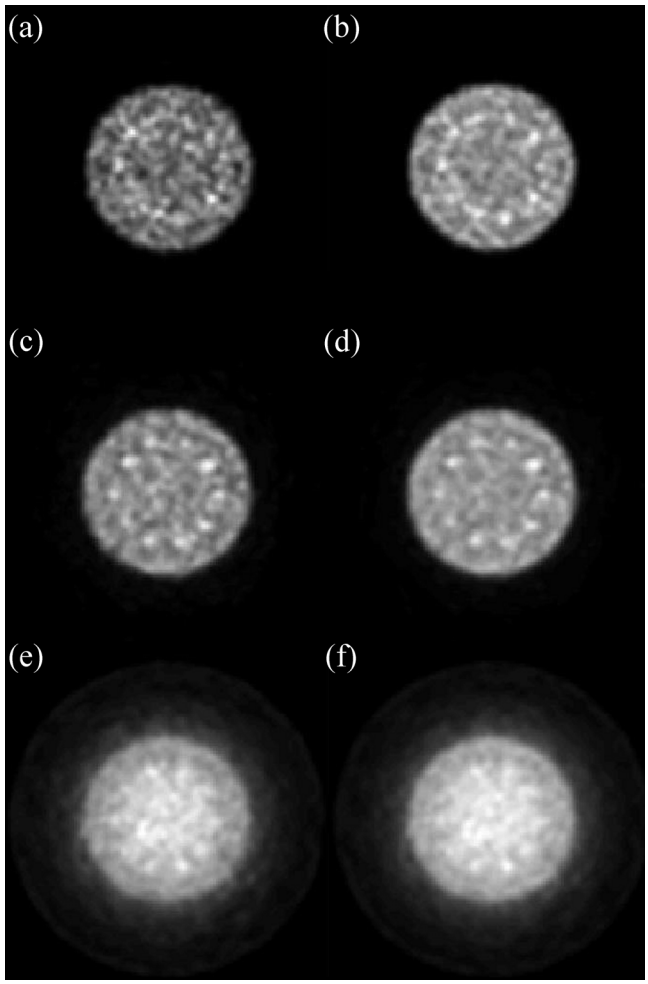

Fig. 3 a-f. Images which are reconstructed without model-based compensation. The left column shows reconstructions with scatter correction, and the right column is without scatter correction. a-b: MEGP collimator, c-d: ELEGP collimator, e-f: LEGP collimator. The LEGP images are reconstructed without attenuation correction.

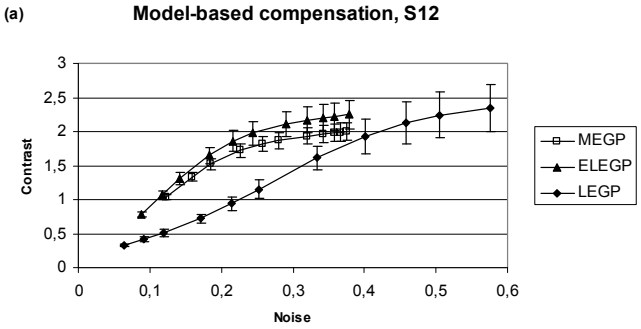

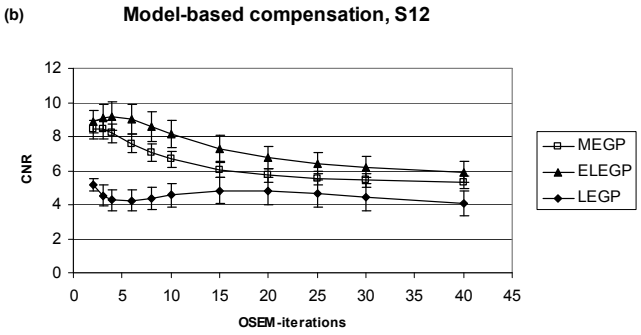

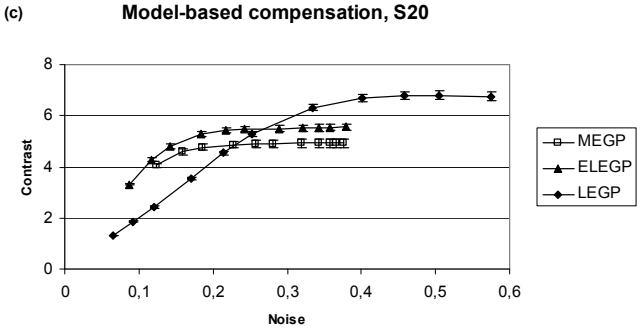

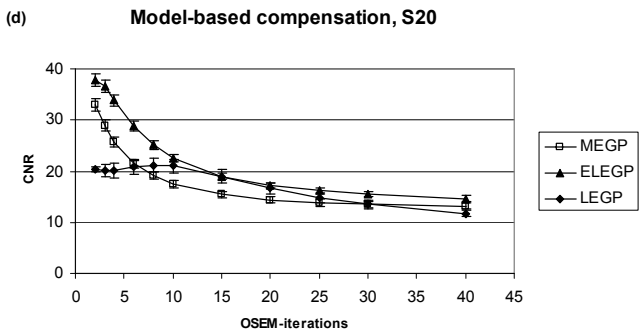

Fig. 4 a-d: Contrast and CNR for the simulated phantom spheres for reconstructions with model-based compensation. The error bars show the standard errors for the spheres.

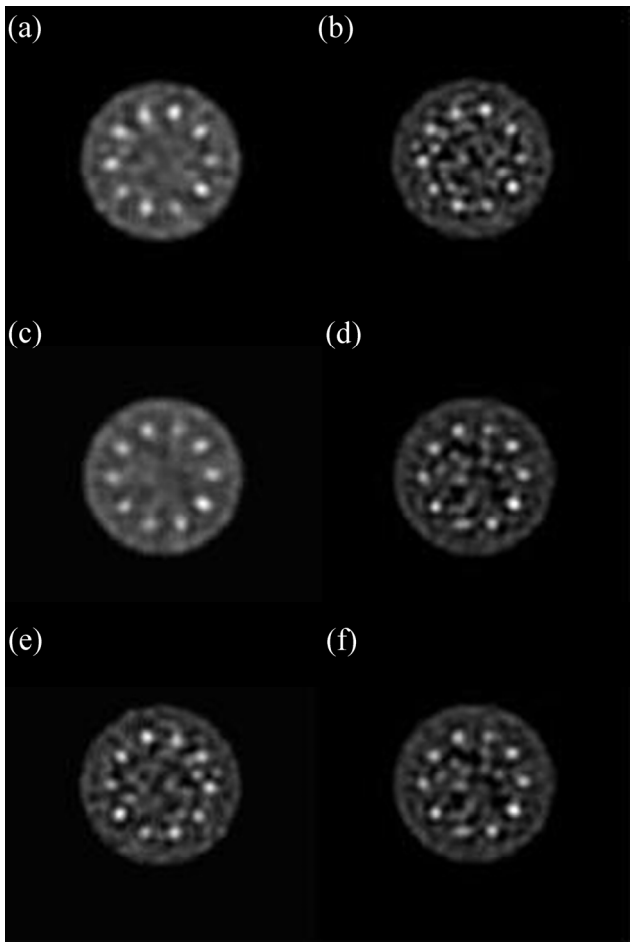

Fig. 5 a-f. Images which are reconstructed with model-based compensation. a-b: MEGP collimator, c-d: ELEGP collimator, e-f: LEGP collimator. The left column shows maximum CNR (MEGP: 3 iterations, ELEGP: 4 iterations, LEGP: 15 iterations), and the right column shows maximum contrast (all collimators: 40 iterations).

Table I Collimator specifications from the Infinia data sheet. The sensitivity values are determined from SIMIND simulations.

	MEGP	ELEGP	LEGP
Hole diameter (mm)	3.0	2.5	1.9
Hole length (mm)	58	40	35
Septal thickness (mm)	1.05	0.4	0.2
System resolution (mm) (^{99m}Tc)	9.4	10.3	9.0
Sensitivity (cps/MBq) (^{111}In, without septal penetration)	104	206	171
Sensitivity (cps/MBq) (^{111}In, including septal penetration)	115	423	1578

Table II Attenuation coefficients for water (cm^{-1}) used for the cylindrical attenuation map.

	MEGP	ELEGP	LEGP
OSEM with scatter correction (cm^{-1})	0.138	0.041	0
OSEM without scatter correction (cm^{-1})	0.092	0.033	0
OSEM with model-based compensation (cm^{-1})	0.138	0.138	0.138